Measurement of residual stress by load and depth sensing indentation with spherical indenters

J.G. Swadener
Oak Ridge National Laboratory, Metals and Ceramics Division, P.O. Box 2008, MS-6093, Oak Ridge, Tennessee 37831-6093, and the University of Tennessee, Department of Materials Science and Engineering, Knoxville, Tennessee 37996-2200

B. Taljat
STEEL Group 31054 Motto di Livenza, Travois, Italy, and Faculty of Mechanical Engineering, University of Ljubljana, Slovenia

G.M. Pharr
Oak Ridge National Laboratory, Metals and Ceramics Division, P.O. Box 2008, MS-6093, Oak Ridge, Tennessee 37831-6093, and the University of Tennessee, Department of Materials Science and Engineering, Knoxville, Tennessee 37996-2200

(Received 4 January 2001; accepted 26 April 2001)

A new experimental technique is presented for making measurements of biaxial residual stress using load and depth sensing indentation (nanoindentation). The technique is based on spherical indentation, which, in certain deformation regimes, can be much more sensitive to residual stress than indentation with sharp pyramidal indenters like the Berkovich. Two different methods of analysis were developed: one requiring an independent measure of the material's yield strength and the other a reference specimen in the unstressed state or other known reference condition. Experiments conducted on aluminum alloys to which controlled biaxial bending stresses were applied showed that the methods are capable of measuring the residual stress to within 10–20% of the specimen yield stress. Because the methods do not require imaging of the hardness impressions, they are potentially useful for making localized measurements of residual stress, as in thin films or small volumes, or for characterization of point-to-point spatial variations of the surface stress.

I. INTRODUCTION

The effects of residual stress on hardness measurement were first demonstrated in 1932 independently by Kokubo[1] and Kostron.[2,3] Twenty years later, Sines and Carlson suggested that these effects could be used to locally measure the residual stresses in the surface of a metal.[4] Numerous studies have since been conducted to examine the relationship between hardness measurement and residual stress.[5–12] In general, hardness decreases with tensile stress and increases with compressive stress, although the effects of compression are often not as large as tension and sometimes not observed. These phenomena are qualitatively explained by simple principles of plasticity. Since the principal stress of greatest magnitude imposed by indentation is compressive and directed normal to the surface of the specimen, a residual tensile stress parallel to the surface increases the magnitude of the local Mises stress, thereby enhancing plastic deformation and reducing the hardness.[4,13] Conversely, if the material is stressed compressively parallel to the surface, the Mises stress is reduced and the hardness is increased.

To date, the development of hardness testing as a tool for measuring residual stress has been based largely on conventional Rockwell testing and Vickers microhardness testing. In these methods, the hardness is deduced either directly from optical measurement of the size of hardness impression or indirectly from the total depth of penetration and the known geometry of the indenter. In contrast, much attention has recently focused on load- and depth-sensing indentation, commonly referred to as nanoindentation, in which properties are deduced from analyses of indentation load–displacement data. Nanoindentation has proven particularly useful in probing the properties of thin films since indentations as shallow as a few nanometers can be used to make measurements. Since thin films are often subjected to large residual stresses, it is natural to ask whether nanoindentation techniques can be developed to measure these stresses. Nanoindentation could also be useful in materials in which point-to-point spatial variations of the surface stress are of interest, e.g., in small second phase particles or in the heat-affected zone of a weld or braze.

A study of the influences of sample stress on nanoindentation hardness measurement with a sharp Berkovich triangular pyramidal diamond indenter was recently reported by Tsui *et al.*[13] The study revealed that the hardness determined by standard nanoindentation techniques is indeed affected by stress, increasing in compression and decreasing in tension in a manner much like that observed in Rockwell and Vickers testing. However, subsequent finite element simulations revealed that the changes in hardness are not real, but rather a testing artifact caused by changes in contact area induced by variations in the pileup geometry, which are not accounted for in the nanoindentation data analysis procedures.[14] Moreover, it was found that the magnitudes of the apparent hardness changes are too small to be of practical use in the measurement of residual stress (hardness changes of less than approximately 10%) and are limited to materials in which pileup is large, i.e., soft metals that do not appreciably work harden.[15]

A theoretical foundation for these observations has recently been proposed by Suresh and Giannakopoulos.[16] Based on their theory, the authors outline a simple method for measuring residual stress with sharp geometrically similar indenters like the Berkovich. The proposed method is based on the difference in contact area of stressed and unstressed materials indented to the same depth, which in principle can be determined by imaging the contact impression or through measurement of the contact stiffness from the indentation load–displacement data (since the contact area is related to the contact stiffness by a simple expression involving the elastic modulus.) However, because the influence of residual stress on the contact area is relatively small, it is not clear that the method can be practically applied except when the residual stress is near the yield stress. No experimental verification of the method was provided.

Taljat and Pharr have recently suggested that much larger effects from residual stress can be measured using nanoindentation with blunt, spherical indenters.[17] Specifically, they have reported the results of a finite element study showing that indentation load–displacement behavior in the transition regime between elastic contact at small loads and fully developed plastic contact at large loads (the so-called elastic–plastic transition) is affected by residual stress in a potentially measurable way.[17] Relevant results of the study are shown in Figs. 1 and 2. In these plots, the horizontal axis is a measure of the extent of indenter penetration into the sample as characterized by the contact radius a normalized in a nondimensional form involving the effective elastic modulus $E_e = E/(1-\nu^2)$ (E is Young's modulus and ν is Poisson's ratio), the yield stress σ_y, and the radius of the rigid spherical indenter R. The nondimensional parameter $E_e a \sigma_y R$ has been used for plotting because Johnson proposed that it would yield an approximately universal curve.[18,19] For large-scale contacts, Taljat and Pharr[17] found that the parameter $2E_e h_c/\sigma_y a$, where h_c is the contact depth, produced a more universal curve, but we use Johnson's suggestion for simpler comparison to earlier work, since the difference between the two parameters is small for the small scale contacts ($a < 0.15\,R$) investigated herein. The plots in Figs. 1 and 2 include simulation results for three different levels of applied biaxial stress: a large tension $\sigma^R = 0.9\,\sigma_y$, a large compression $\sigma^R = -0.9\,\sigma_y$, and a stress-free condition $\sigma^R = 0$.

Figure 1 shows how the mean contact pressure p_m is influenced by the biaxial residual stress. Note that for both very small and very large contacts (or loads), p_m is essentially independent of the stress. Small-scale contact is not affected by residual stress because deformation is in the Hertzian elastic regime, and large scale contact is unaffected because plasticity is fully developed and deformation is dominated by the large plastic strains around the indenter. However, in the intervening elastic–plastic transition, the indentation behavior depends on both the magnitude and the sign of the residual stress.

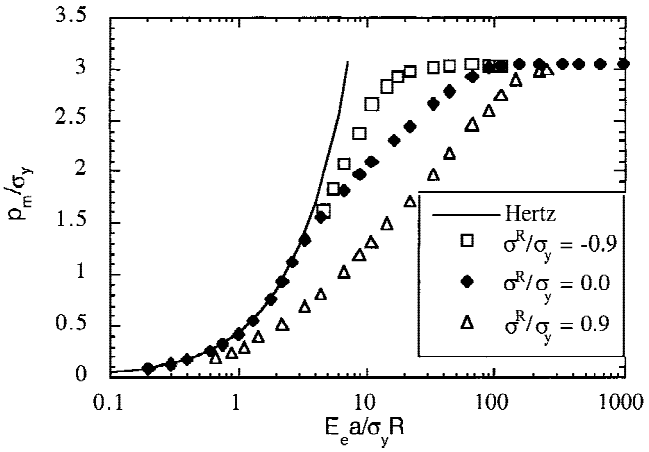

FIG. 1. FEA prediction of the effect of residual stress on mean pressure (from Ref. 17).

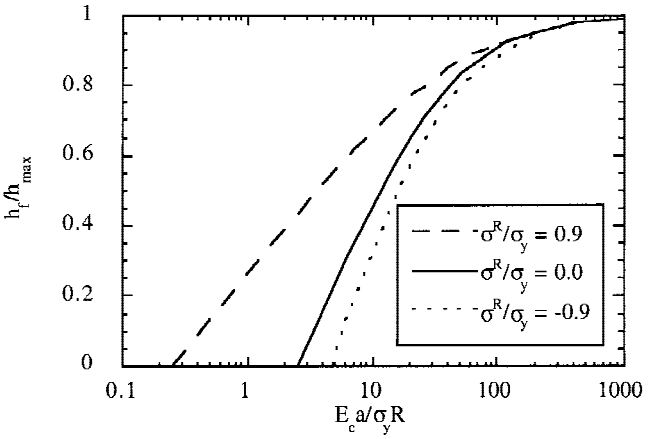

FIG. 2. FEA prediction of the effect of residual stress on the elastic recovery parameter h_f/h_{max} (from Ref. 17).

Tensile stresses reduce the mean pressure because they promote yielding and plastic flow by increasing the local Mises stress, whereas compressive stresses have the opposite effect.

Figure 2 demonstrates the effect of biaxial stress on the indentation load–displacement behavior as characterized by the ratio of the final depth of penetration h_f to the maximum depth of penetration h_{max}. The parameter h_f/h_{max}, which varies in the range $0 \leqslant h_f/h_{max} \leqslant 1$, is an experimentally accessible measure of the relative amount of elastic and plastic deformation during contact. When $h_f/h_{max} = 0$, deformation is fully elastic, whereas when fully plastic contact is achieved, h_f/h_{max} approaches a value slightly less than 1 (note that $h_f/h_{max} = 1$ only when there is no elastic deformation in the material, i.e. for a rigid-plastic solid). The point on the abscissa at which h_f/h_{max} first increases above zero represents initial yielding in the specimen. The plot shows that initial yielding is significantly affected by residual stress, as would be expected based on the reduction or enhancement of the Mises stress. The results also show that h_f/h_{max} is affected by residual stress well into the elastic–plastic transition regime and may thus serve as a convenient experimental parameter for measuring the residual stress.

Based on these observations and the principles underlying them, techniques for measuring residual stress from nanoindentation load–displacement data obtained with spherical indenters are presented in this paper. Two separate methods are developed that can be used in different circumstances depending on what information is independently available to the investigator. The first method requires that the yield strength of the material be known, while the second method requires the testing of a specimen in a known reference state of stress, e.g., stress free. The measurement capabilities of the methods are assessed by nanoindentation experiments conducted on aluminum alloys to which controlled biaxial stresses could be applied by axisymmetric bending of circular disks. The experiments show that measurements of residual stress to within ±10–20% of the yield stress are possible.

II. THEORY

The methods developed in this work rely heavily on mathematical expressions describing deformation in the elastic–plastic transition during spherical indentation, particularly those relating the mean contact pressure to the size and/or depth of the contact. The most important of these equations are now briefly reviewed.

Initial contact between a spherical indenter and an isotropic elastic–plastic material occurs at low stress in the elastic regime. As long as the radius of the contact a is small compared to the radius of the indenter R the classical theory developed by Hertz can be used to describe the deformation behavior up to the load at which yielding first occurs.[20] The equation relating the total depth of penetration h to the contact radius a for Hertzian contact is

$$h = \frac{a^2}{R} \quad , \tag{1}$$

for which the contact geometry is detailed in Fig. 3. The total applied load P is related to h by

$$P = \tfrac{4}{3} E_e R^{1/2} h^{3/2} \quad , \tag{2}$$

where E_e is the effective elastic modulus given by

$$E_e = \left(\frac{1 - \nu_i^2}{E_i} + \frac{1 - \nu_s^2}{E_s} \right)^{-1} \quad . \tag{3}$$

In Eq. (3), E_i and ν_i are the elastic modulus and Poisson's ratio, respectively, of the indenter, and E_s and ν_s are the same quantities for the material. From Eqs. (1) and (2), the mean contact pressure, p_m under the indenter during elastic deformation can be related to the contact radius by

$$p_m = \frac{P}{\pi a^2} = \frac{4E_e a}{3\pi R} \quad , \tag{4}$$

where a positive value of p_m indicates that the pressure is compressive.

Hertzian contact is an axisymmetric problem for which the state of stress can be thought of as a combination of hydrostatic compression and biaxial tension in the r and θ directions. When there is no preexisting stress in the material, the maximum shear stress occurs

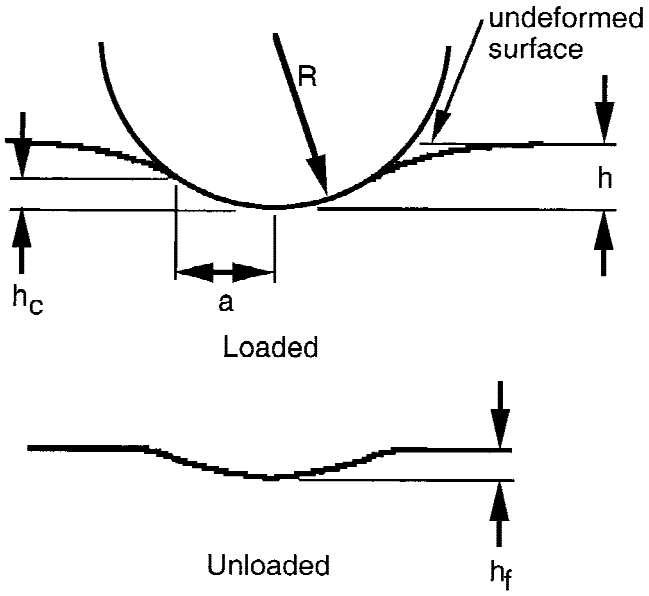

FIG. 3. Spherical indentation geometry.

beneath the surface along the axis of indentation (the z axis). As the load is increased, the yield criterion for the material is reached, and a small plastic zone develops beneath the surface. With further increases in load, the plastic zone grows until it reaches the surface and spreads beyond the area in contact with the indenter. After yielding has initiated, the Tabor relation[21] can be used to relate the mean pressure to the effective flow stress σ_f through

$$p_m = \psi\sigma_f \quad , \tag{5}$$

where ψ is a constraint factor that varies with the relative depth of penetration (or, alternatively, with the ratio a/R) and σ_f is the flow stress at an effective strain defined by $\epsilon_f = 0.2a/R$. The constraint factor, which depends on the elastic–plastic behavior of the material, represents the resistance to further yielding due to the effects of hydrostatic constraint on plasticity. At the onset of yielding, Johnson[18] showed using either the Tresca or the von Mises yield criterion that $\psi = 1.07$ (often rounded to 1.1). The value of ψ increases as the plastic zone grows, and Tabor suggested that when the plastic strains in the vicinity of the contact are large compared to the elastic strains, the constraint factor reaches a plateau value of $\psi = 2.8$.[21] The spherical cavity model proposed by Johnson is often used to describe the development of the constraint factor during the transition from the initiation of yielding to the fully plastic condition.[18,19] For an elastic–perfectly–plastic material, Johnson's model gives

$$\psi = C_1 + C_2 \ln\left\{\frac{E_e a}{3\sigma_y R} + \frac{2(1-2\nu)}{3(1-\nu)}\right\} \quad , \tag{6}$$

where $C_2 = 0.67$ and $C_1 = 0.86$ for $\nu_s = 0.25$ and $C_1 = 0.67$ for $\nu_s = 0.5$. Experimental results have confirmed the general form of Eq. (6),[22,23] but the constants C_1 and C_2 vary from the predictions of the model in a manner that is material dependent.

When a biaxial residual stress σ^R is present in the material, Taljat and Pharr have shown by finite element analysis (FEA) that the onset of yielding is determined by the superposition of the biaxial and Hertzian stresses.[17] As long as yielding initiates below the surface along the axis of symmetry, the yield condition is given by

$$p_m = 1.07\,(\sigma_y - \sigma^R) \quad , \tag{7}$$

where the contact pressure p_m is positive and the residual stress σ^R is positive for tension and negative for compression. Equation 7 follows directly from Eq. (5) by noting that a tensile residual stress will reduce the flow stress at yielding by an amount exactly equal to σ^R, that is, $\sigma_f = \sigma_y - \sigma^R$, and that the constraint factor at yielding is $\psi = 1.07$.

Eq. (7) forms the basis of one of the methods developed here for measuring the residual stress. The method requires that the yield stress be known and that the contact pressure at the onset of yielding be determined experimentally. The method we propose for measuring the contact pressure at yield is to extrapolate experimental data of the form of that in Fig. 2 to $h_f/h_{max} = 0$. The contact radius determined from the extrapolation can then be used in Eq. (4) to determine the contact pressure at yielding, which can then be used in Eq. (7) to determine σ^R. A complication arises when the residual stresses are large and compressive, since the physical location in the specimen at which yielding begins can switch from beneath the surface, as described by the classical Hertzian theory, to the contact periphery at the surface.[17] Using finite element analysis for a material with $\nu_s = 0.3$, Taljat and Pharr found that the switch occurs when $\sigma^R < -0.75\,\sigma_y$ and that the associated yielding takes place at slightly lower indentation pressures than those calculated by Eq. (7).[17] However, they also found that the yield pressure is still adequately estimated by the extrapolation procedure suggested above. An analytical justification for the change in the yielding location is given in Appendix A.

The second method for determining the residual stress relies on an experimental observation made during the course of this work concerning the influence of residual stress on the mean contact pressure in the elastic–plastic transition regime. This method will be developed and discussed after the necessary experimental results have been presented.

III. PROCEDURES

A. Experimental

Indentation with continuous load and depth measurement (nanoindentation) was conducted on polished disks of commercial aluminum alloys. The specimens were mounted in bending fixtures, which applied either compressive or tensile biaxial stress to the specimen surface. Nanoindentation was conducted using a synthetic sapphire spherical indenter.

To evaluate a large range of yield strength and ultimate strength in similar materials, three common precipitation hardened commercial aluminum alloys were chosen for study: 2024-T3, 6061-T6, and 7075-T6. The mechanical properties of these materials as measured in uniaxial tension are listed in Table I.[24] The 6061-T6 and 7075-T6 alloys both show little work hardening, but their yield strengths differ by a factor of 1.8. The 2024-T3 alloy exhibits a greater work hardening and has an intermediate yield strength.

Circular disks 50 mm in diameter and 3.2 mm thick were fabricated from sheets of the three alloys. The specimen surfaces to be indented were mechanically

TABLE I. Specimen mechanical properties (from Ref. 24).

Alloy	0.2% offset yield strength (MPa)	Ultimate tensile strength (MPa)	Ultimate elongation in tension (%)	Elastic modulus (GPa)	Poisson's ratio, ν	Work hardening coefficient, k (MPa)	Work hardening exponent, n
2024-T3	345	483	18	73.1	0.33	777	0.10
6061-T6	276	310	12	69.0	0.33	377	0.039
7075-T6	503	572	11	71.7	0.33	724	0.051

polished with successively finer grit materials, and finished with 0.1-μm diamond paste. The specimens were then loaded in axisymmetric bending by the apparatus shown schematically in Fig. 4. Indentation experiments were conducted on the upper biaxially stressed surface within a radius 3 mm from the center. Since the indented region was two to three specimen thicknesses away from the loading points, St. Venant's principle indicates that the tested region was in a state of approximately pure biaxial bending. The indenter penetrated only to a maximum of 1.5 μm into the surface, so the state of stress was effectively constant with depth. A strain gauge rosette attached to the center of the lower specimen surface was used to measure the strains applied by the bending fixture. At higher levels of applied bending load, some plastic yielding was noted by comparing the strains measured during loading in the fixture with the strains after unloading. The in-plane stresses were calculated from the total accumulated strains. Unloading was assumed to be elastic, since the maximum accumulated plastic strain was always less than the elastic strain. To avoid residual stress in the indented surface, bending loads were applied at progressively larger magnitudes, and separate specimens were used for tensile and compressive loading.

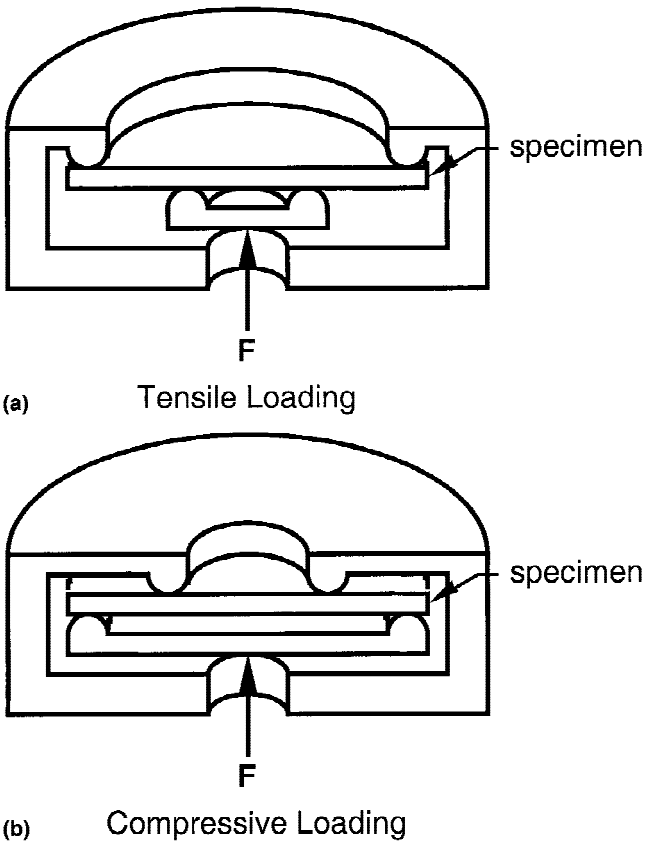

FIG. 4. Schematic of axisymmetric bending apparatus.

Indentation experiments were conducted using a nanoindentation system with displacement and load resolutions of 0.16 nm and 0.3 μN, respectively. The indenter tip was fabricated from a polished synthetic sapphire sphere pressed into a stainless steel mount and brazed in place. The spherical tip was calibrated over depths from 50 to 500 nm by nanoindentation of single crystal sapphire and fused quartz specimens in the elastic regime.[25] The calibrations yielded a tip radius of 69 μm and a machine stiffness of 9.0×10^9 N/m. These values were found to work well for depths up to 1500 nm (1.5 μm) based on nanoindentation measurement of the elastic moduli of the aluminum alloys. Although the spherical sapphire indenter is elastically anisotropic, its effective indentation modulus, $E_i/(1 - \nu_i^2)$ in Eq. (3), as determined by Swadener and Pharr,[26] falls over a fairly narrow range: 412 to 438 GPa. The mean value of 425 MPa was used to analyze the Experimental results.

Nanoindentation was conducted in load control using a five-step procedure: loading at a constant rate to a prescribed maximum load, a 30-s hold at constant load, unloading at the same rate as loading to 10% of the maximum load, a 100-s hold, and complete unloading. During the 100-s hold period, displacements were measured to determine the thermal drift of the apparatus. Displacement measurements were corrected for thermal drift, which was generally found to be less than 0.03 nm/s. Four maximum load values (20, 60, 200, and 600 mN) were used for each applied biaxial stress. Ten experiments were performed at each load, although some were not successful due to improper detection of the surface.

B. Finite element simulations

A limited number of finite element analyses were conducted using procedures identical to those employed by Taljat and Pharr[17] to augment earlier results. Simulations were conducted using the commercial finite element code ABAQUS (Hibbitt, Karlsson, and Sorensen, Inc., 1996) employing axisymmetric analysis for a rigid

spherical indenter. The diameter of the indenter was varied over the range of 2 to 25 mm depending on the desired range of the analysis. The specimen measured 40 mm in diameter and 20 mm high and was composed of 1746 linear four-node elements. Displacements on the lower specimen boundary were fixed in the *z*-direction and unconstrained in the *r*-direction, while the upper and outer boundaries were unconstrained in all directions. A friction coefficient of 0.2 was used for contact between the indenter and the specimen.

The analysis used an isotropic elastic–plastic constitutive model for the specimen. The von Mises yield criterion and a stationary yield surface were employed. The specimen yield strength and elastic modulus were varied, but a Poisson's ratio of 0.3 was used throughout. Prior to simulation, uniform tractions were applied, which resulted in equal biaxial stress throughout the specimen. Simulations were run over a wide range of loads for various material property combinations so that the analysis spanned elastic to fully plastic contact.

C. Measurement of indentation parameters

The methods developed in this work are premised on accurate measurement of four indentation parameters: (i) the peak indentation load P_{max}, (ii) the total depth of penetration h_{max}, (iii) the residual (or final) depth of the contact h_f, and (iv) the contact radius a. Both P_{max} and h_{max} were obtained directly from the indentation load–displacement data. In principle h_f could also have been determined from the load–displacement curves, but since data during the final stages of unloading were sometimes of questionable accuracy and/or obscured by the constant load hold period near the end of the test (during which the thermal drift rate is measured), an alternative procedure was adopted. The procedure is based on the assumption that the unloading process can be modeled as the elastic unloading of a sphere of one radius R_1 from a spherical contact impression of another radius R_2. Under these circumstances, Hertzian contact theory applies, and the unloading data may be described by the modified form of Eq. (2):

$$P = \tfrac{4}{3} R_e^{1/2} E_e (h - h_f)^{3/2} \quad , \tag{8}$$

where R_e is an effective radius related to R_1 and R_2 through $R_e = (1/R_1 - 1/R_2)^{-1}$.[20] Values of h_f were determined by curve fitting the upper 90% of the unloading data to this equation, i.e., from peak load down to the drift hold segment. Since the value of R_2 was unknown, it, too, was treated as an unknown in the regression analysis. The quality of the curve fits was good (correlation coefficient, $r > 0.999$), suggesting that the unloading behavior is indeed accurately modeled by the Hertzian theory.

The indentation contact radius a could not be measured directly from the *P-h* data but was deduced from it by well-established methods. The method used in this study is that developed by Francis[22] and Field and Swain,[27] in which the depth of penetration over which contact occurs (h_c in Fig. 3) is modeled to consist of elastic and plastic components. The plastic component is the residual depth of the impression h_f. Using Hertzian contact theory, the elastic component is just half the difference between the total depth (h_{max}) and the residual depth (h_f), as noted by Francis.[22] Therefore, the contact depth can be written in the form:[27]

$$h_c = \tfrac{1}{2}(h_{max} + h_f) \quad . \tag{9}$$

Once h_c is determined, the contact radius follows from the spherical indenter geometry through

$$a = (2Rh_c - h_c^2)^{1/2} \quad . \tag{10}$$

Alternatively, the contact depth could have been determined from the contact stiffness at the beginning of the unloading segment using the Oliver–Pharr method of load–displacement data analysis.[28]

In addition to the four measured parameters listed above, one of the methods requires an estimation of the depth dependence of the mean contact pressure p_m. This follows quite simply from the other measured parameters since

$$p_m = \frac{P_{max}}{\pi a^2} \quad . \tag{11}$$

Much of the data obtained in this study was analyzed and plotted as a function of the nondimensional contact radius $E_e a/\sigma_y R$. To determine this parameter, the effective modulus E_e was computed from Eq. (3) using the relevant material data in Table I and assuming that the effective indentation modulus for the sapphire indenter is $E_i/(1 - \nu_i^2) = 425$ MPa.[24] Values of ν and σ_y were taken from Table I, and the indenter radius $R = 69$ μm determined from calibration procedures was employed.

IV. RESULTS AND DISCUSSION

A. Influence of stress on indentation load–displacement data

The experiments conducted in this study showed that there is indeed a significant effect of biaxial stress on nanoindentation load–displacement data obtain with spherical indenters in the elastic–plastic transition regime. Figure 5 shows several load–displacement curves for 6061-T6 aluminum, which is typical of the materials examined in this study. Noting that the solid curve represents the behavior of an essentially unstressed material,

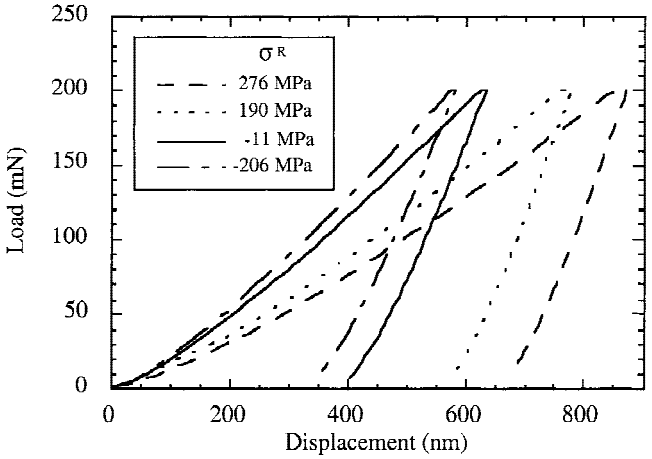

FIG. 5. Typical load–displacement results for spherical indentation of 6061-T6 Al for various biaxial stress cases.

it is apparent that biaxial tension tends to stretch out the curves to larger depths, while compressive stresses compress the curves to smaller depths. Thus, at a given indentation load, the total depth of penetration h_{max} is much greater for a material stressed in tension than an unstressed specimen or one stressed in compression. The final depth h_f exhibits similar behavior, implying that plastic deformation is enhanced by tension and diminished by compression. These observations are qualitatively in agreement with previous results obtained using Brinell hardness testing.[9]

Two methods were developed for measuring the biaxial stress, which utilize data from load–displacement curves such as those in Fig. 5. One relies on the influences of residual stress on the onset of yielding, and the other on the variation of the contact pressure with residual stress for data obtained in the elastic–plastic transition.

B. Method I: Onset of yielding

The first method for measuring the residual stress is based on the principles outlined at the end of Sect. II. The basic idea is to obtain indentation data at a variety of indentation depths and loads in the elastic–plastic transition and to extrapolate from a plot of h_f/h_{max} versus $E_e a/\sigma_y R$ like that in Fig. 2 to determine $(E_e a/\sigma_y R)_0$, the value of the nondimensional contact radius at the onset of yielding. The importance of this measured parameter is seen by combining Eqs. (4) and (7) to obtain:

$$\frac{\sigma^R}{\sigma_y} = 1 - \frac{3.72}{3\pi}\left(\frac{E_e a}{R\sigma_y}\right)_0 \quad . \tag{12}$$

Equation 12 shows that if an independent estimate of σ_y is available, the residual stress can be determined by simple experimental measurement of $(E_e a/\sigma_y R)_0$.

The procedure we propose for measuring $(E_e a/\sigma_y R)_0$ is based on the form of the finite element results in Fig. 2. Since the abscissa of this plot is $E_e a/\sigma_y R$, the value at which plasticity commences as indicated by h_f/h_{max} first increasing above zero is the desired parameter. However, direct determination of this point is difficult because yielding generally commences beneath the surface, and its effect on the indentation displacements is difficult to detect in the early stages of plasticity. Moreover, in the experiments conducted in this study, yielding initiated at very small depths where the depth measurement was imprecise. Thus, instead of attempting to determine the onset of yielding directly, we note that h_f/h_{max} as shown in Fig. 2 initially increases in an approximately logarithmic manner with $E_e a/\sigma_y R$. Therefore, the onset of plasticity can be estimated by extrapolating experimental results obtained at various indentation depths to $h_f/h_{max} = 0$ using least squares regression curve fits of the form $h_f/h_{max} = A_1 + A_2 \log\{E_e a/\sigma_y R\}$. When applied to the finite element results, this procedure gave values of $(E_e a/\sigma_y R)_0$ accurate to within 2%, even when the onset of yielding shifted to the edge of the contact at large compressive biaxial stresses ($\sigma^R = -0.9\,\sigma_y$).

Figures 6 and 7 present nanoindentation data obtained to implement and examine the proposed method for two of the aluminum alloys: 2024-T3 (Fig. 6) and 6061-T6 (Fig. 7). Data for the 7075-T6 alloy are not included because hard particulates in the material made it difficult to obtain smooth surfaces at the micron scale. The resulting surface roughness led to difficulties in determining the true location of the surface and produced a large degree of scatter in the results at the small to moderate depths, which are most important in the extrapolation. In the experiments, values of h_f/h_{max} were kept to less than 0.7 by

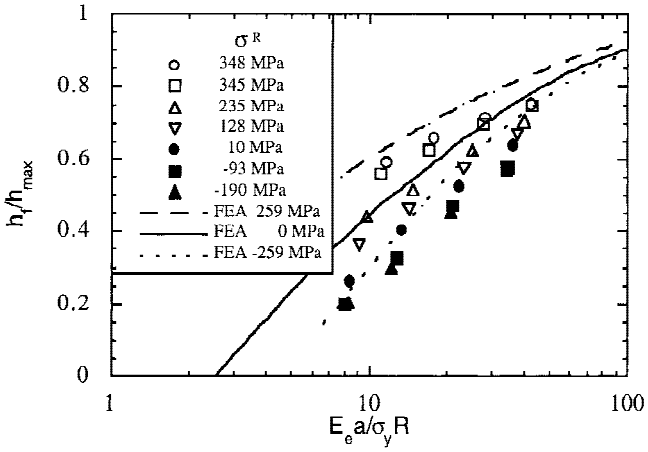

FIG. 6. Effect of biaxial stress on residual depth as a function of contact radius for spherical indentation in 2024-T3 Al. Mean values are shown. The standard deviation in $h_f/h_{max} = 0.02$.

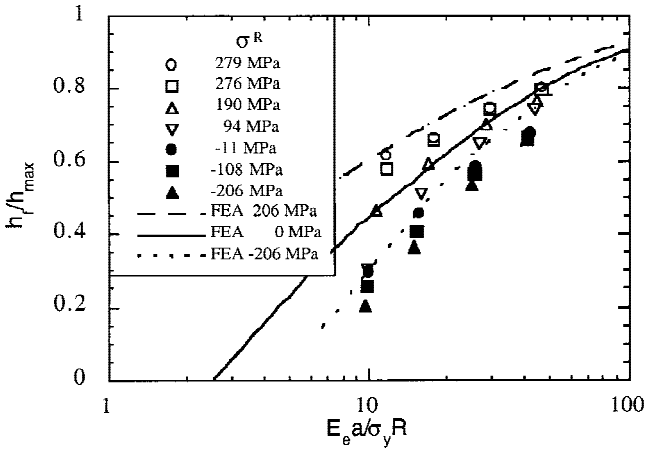

FIG. 7. Effect of biaxial stress on residual depth as a function of contact radius for spherical indentation in 6061-T6 Al. Mean values are shown. The standard deviation in $h_f/h_{max} = 0.02$.

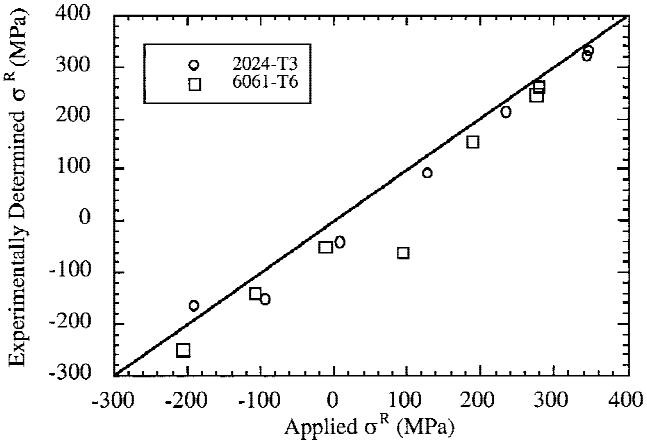

FIG. 8. Values of biaxial stress determined by extrapolation to the onset of yielding in spherical indentation experiments in 2024-T3 Al and 6061-T6 Al.

careful choice of experimental conditions to ensure that the data reside in the elastic–plastic transition regime where the effects of residual stress are most pronounced.

Included with the data in Figs. 6 and 7 are predictions of several finite element simulations for elastic–perfectly-plastic materials having the same yield stresses as the experimental materials. While the general trends in the finite element results are observed in the experimental data, there are notable differences in the numerical predictions. For example, for the 2024-T3 data in Fig. 6, the simulations and experiments differ by a factor of about 1.3 in the $E_e a/\sigma_y R$ values for small contacts and by a factor of approximately 1.6 for larger contacts. Similar differences are observed in Fig. 7 for the 6061-T6. These discrepancies are probably due to differences between the idealized plastic behavior assumed in the finite element simulations and the behaviors of the real materials, which exhibit some work hardening. A preliminary finite element analysis for 2024-T3, which includes linear work hardening, is in closer agreement with the experimental results. However, further studies are needed to quantify the effects of work hardening.

With the values of yield stress given in Table I and the values of $(E_e a/\sigma_y R)_0$ obtained from the experimental data in Figs. 6 and 7 by the logarithmic extrapolation procedure, biaxial residual stresses were predicted by Eq. (12). Results are summarized in Fig. 8, where the experimentally determined values of σ^R are plotted as a function of the known biaxial stress obtained from the strain gage measurements. The agreement is generally good. The standard error for the σ^R values is 37 MPa for the 2024-T3 (11% of the yield strength), and 67 MPa for the 6061-T6 (24% of the yield strength). The larger error for the 6061-T6 is caused mainly by one outlying data point, that at an applied stress value of 94 MPa.

Comparison of the data points in Fig. 8 to the solid line representing a perfect prediction shows that the measured biaxial stresses are systematically lower than expected. The slight bias toward the compression side by an average of 40 MPa may be due to compressive residual stress near the surface caused by mechanical polishing. If corrections are made for this bias, the results are generally within 10% of the yield strength for each material.

One limitation of this method is that for tensile biaxial stresses, the extrapolation cannot predict a value of σ^R greater than σ_y because the logarithmic extrapolation cannot extend below zero. This is not a concern for the range of biaxial stress examined in this study but may be important for materials with a large capacity for work hardening. Another limitation is that the yield stress must be known independently. In practice, this limitation can be overcome if a specimen of the material in a known state of stress is available, e.g., stress free, since indentation experiments like those in Figs. 6 and 7 conducted in the reference material could be used in conjunction with Eq. (12) to estimate σ_y. An overestimation of σ_y by 10% would lead to predictions of biaxial tensile stress that are 10–15% higher and predictions for compressive stress that are 5–10% lower. An underestimation of σ_y would have the opposite effect.

Conceivably, this method could be extended to cases of uniaxial stress by calculating the criteria for the onset of yielding in uniaxially stressed materials. Mroz[29] recently proposed using oblique indentation in various directions to distinguish between uniaxial and biaxial residual stresses.

C. Method II: Influence of residual stress on contact pressure

A second method for measuring the biaxial stress is based on an important experimental observation made during the course of this investigation. In Fig. 9, Eq. (11)

was used to plot the 2024-T3 data in Fig. 6 as the mean contact pressure p_m versus the nondimensional contact radius $E_e a/\sigma_y R$. Inspection of this plot reveals that data obtained at different applied biaxial stresses are offset vertically by an amount very close to the magnitude of the applied stress. To further examine this point, the data in Fig. 9 have been replotted as $p_m + \sigma^R$ versus $E_e a/\sigma_y R$ in Fig. 10. The convergence of the data to a single master curve suggests that $p_m + \sigma^R$ is a unique function of $E_e a/\sigma_y R$, that is, $p_m + \sigma^R = f(E_e a/\sigma_y R)$. Note that when $\sigma^R = 0$, the function is given by Eq. 5 or $f(E_e a/\sigma_y R) = \psi\sigma_f$; thus, $f(E_e a/\sigma_y R)$ describes the development of constraint during indentation. These observations suggest that for stressed specimens, Eq. 5 should be rewritten as:

$$p_m + \sigma^R = \psi\sigma_f \quad . \tag{13}$$

Eq. (13) forms the basis of another method for stress measurement. If the variation of $\psi\sigma_f$ with $E_e a/\sigma_y R$ can be established by experiments in a reference material in a known state of stress, then σ^R can be determined from measurements of the indentation contact pressure p_m. From a theoretical perspective, Eq. (13) would be expected to hold as long as the elastic strains are large compared to the plastic strains. Under these conditions, the stresses are largely determined by elastic deformation, and the early-stage growth of the plastic zone and its influences on the indentation behavior may be modeled as if the governing stresses were determined by the superposition of the Hertzian contact stresses and the applied biaxial stress. Strictly speaking, Eq. (13) would be expected to apply only when the form and shape of the plastic zone for the stressed specimen is the same as that for the reference state. However, based on the experimental observations, this does not appear to be a severe limitation.

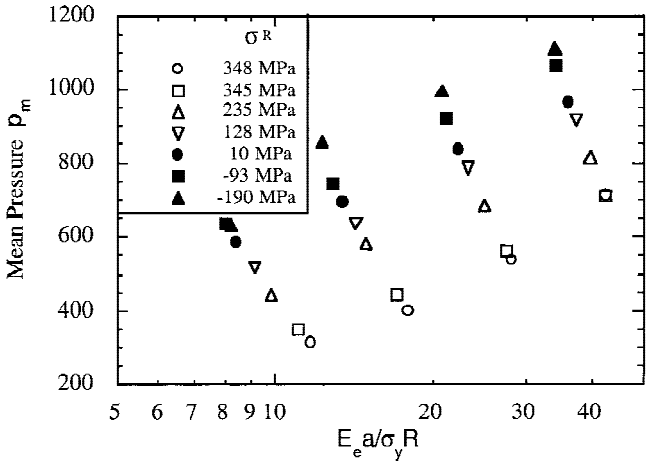

FIG. 9. Effect of biaxial stress on the mean pressure under the indenter as a function of contact radius for spherical indentation in 2024-T3 Al. Mean values are shown. The standard deviation is p_m = 30 MPa.

To further explore these ideas, the variation of the constraint factor $\psi = p_m/\sigma_f$ with $E_e a/\sigma_y R$ was determined for each of the aluminum alloys by experimental measurement at small applied biaxial stresses (σ^R = 10 MPa for 2024-T3; $\sigma^R = -11$ MPa for 6061-T6; $\sigma^R = -4$ MPa for 7075-T6). Following Tirupataiah and Sundararajan,[23] the flow stress was calculated as $\sigma_f = k(0.2a/r)^n$, where k is the work hardening coefficient and n is the work hardening exponent, using the material properties in Table I. Results are plotted in Fig. 11. Interestingly, the variation of ψ for the three alloys is essentially indistinguishable within the experimental uncertainty. While the coalescence of the data to a single curve is not necessary for the proposed method of residual stress analysis, the behavior shown in Fig. 11 could be used as an estimate of the variation of the constraint factor in circumstances where a reference specimen is not available for testing. Values for ψ for

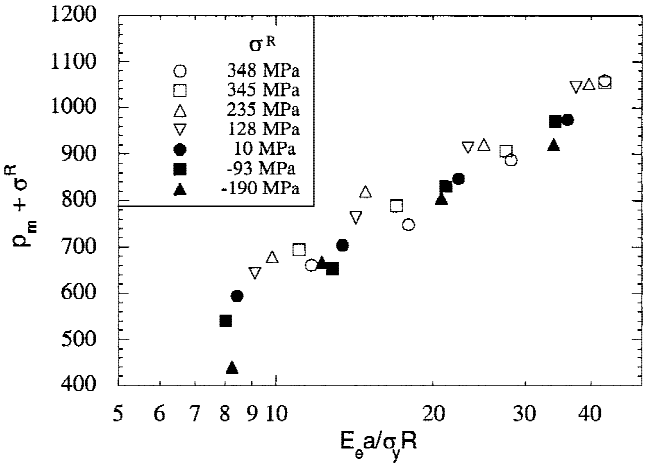

FIG. 10. Data from Fig. 9 replotted as ($p_m + \sigma^R$) versus $E_e a/\sigma_y R$ illustrating convergence of the data to a single curve.

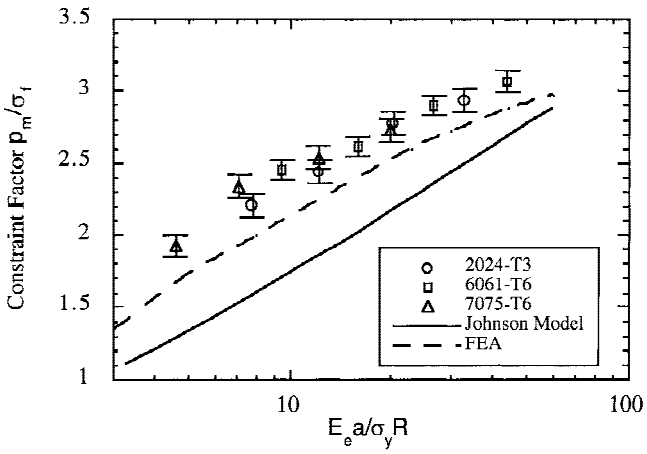

FIG. 11. Variation of the constraint factor with contact radius for spherical indentation of the aluminum alloys in the unstressed condition.

elastic–perfectly-plastic materials determined by finite element analysis also shown in the figure are approximately 0.2 lower than the experimental values. Approximately half of this difference can be attributed to the suspected 40-MPa compressive residual stress in the specimens. There may also be some discrepancy due to differences between the work hardening of the elastic–perfectly-plastic model and the actual work hardening of the specimens. For comparison, the value of ψ predicted by Johnson's expanding cavity model[18,19] is also plotted in the figure, but it is not in good agreement with any of the experimental data. The behaviors of the three Al alloys in the unstressed state are similar to experimental results by Tirupataiah and Sundararajan for peak-aged 7039 Al.[23]

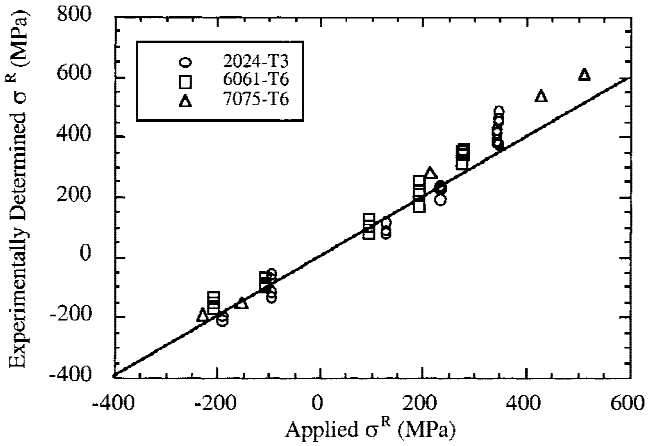

FIG. 12. Values of biaxial stress determined by comparison to a material in the unstressed state in spherical indentation experiments in the aluminum alloys.

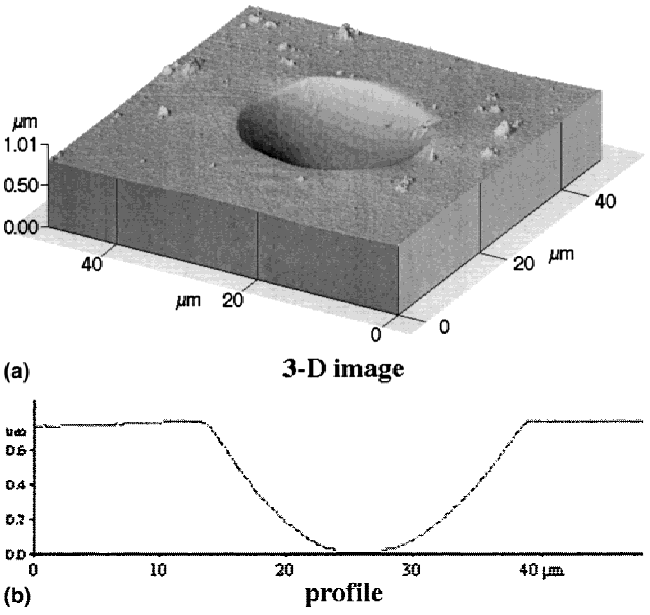

FIG. 13. Contact atomic force microscopy image of a 50-μm-square region in the neighborhood of a 600 mN indentation in 2024-T3 aluminum.

Least squares logarithmic curve fits of the data for each alloy in Fig. 11 were used to describe the dependence of ψ on $E_e a/\sigma_y R$ in the low stress reference condition, and values of σ^R were computed from measurements of the mean contact pressure by means of Eq. (13). The results are shown in Fig. 12. Measurements for the 7075-T6 alloy were limited only to the largest loads and depths ($P_{max} = 600$ mN; $h_{max} = 1500$ nm) due to the aforementioned scatter in results at small to moderate depths caused by surface roughness. For the other two materials, the σ^R values were experimentally determined at all depths for which data were available. The standard errors for the experimental measurement of σ^R were 48, 46, and 75 MPa for the 2024-T3, 6061-T6, and 7075-T6 alloys, respectively, which are 14–17% of the yield strengths. In contrast to the results obtained by method I (extrapolation to the onset of yielding), no bias toward compression was observed, because the measurements were made relative to a reference state which was assumed to be unstressed, i.e., any preexisting stress in the reference specimen due to polishing and surface preparation was not taken into account.

D. Complications due to pileup

One potential difficulty in the general application of these methods is the effect of pileup on the calculated contact radius. Materials that exhibit little work hardening like the aluminum alloys examined here might be expected to exhibit pileup around the indenter, leading to an actual contact area that is larger than that calculated from Eqs. (9) and (10).[15,30,31] Pileup would be greatest for large contacts in materials with little work hardening.

To evaluate the extent of pileup, indented surfaces were examined with atomic force microscopy (AFM). A surface scan in the region near a large, 600-mN indentation in Al 2024-T3 is shown in Fig. 13. While this indentation has a contact depth of 1100 nm, the height of the residual pileup is less than 20 nm, implying that the change in contact area due to pileup is less than 5%. A recent finite element analysis of spherical indentation showed that pileup is minimal in virtually all materials, irrespective of their work hardening behavior, when the contact radius less than 0.1 R.[31] Therefore, the influences of pileup can be avoided by conducting experiments at a/R ratios of less than 0.1.

V. CONCLUSIONS

Biaxial stress has a large effect on spherical indentation experiments conducted in the elastic–plastic transition regime, in agreement with previous observations[9] and predictions.[17] Two methods have been developed to determine the biaxial stress from load- and depth-sensing

indentation experimental results. The methods are accurate to within 10–20% of the specimen yield strength and can be applied to cases of tensile or compressive biaxial stress.

The first method extrapolates spherical indentation data from the post-yield regime to determine the contact radius at the onset of yielding. If the specimen yield strength is known, the biaxial stress can then be determined based on a closed form analytical solution. This method could potentially be extended to cases of uniaxial residual stress, but further study is needed to establish the differences in behavior of uniaxially and biaxially stressed specimens.

The second method requires a specimen in a known stress state (such as stress free), which can be tested as a reference to determine how the indentation constraint factor increases with contact depth (or radius). Using an empirically derived expression relating the biaxial stress to the mean contact pressure and the constraint factor, the residual stress can then be estimated. The second method has the advantage of not requiring the yield strength of the specimen to be known in advance.

The methods can be used to determine residual stress for a wide range of materials which can withstand a moderate degree of indentation without fracture. In this study, effective strains ($0.2\,a/R$) of 1–2% were sufficient to apply the methods and estimate the biaxial stress.

ACKNOWLEDGMENTS

Research at the Oak Ridge National Laboratory SHaRE User Facility was sponsored by the Division of Materials Sciences and Engineering, United States Department of Energy, under Contract No. DE-AC05-00OR22725 with UT-Battelle, LLC.

REFERENCES

1. S. Kokubo, Science Reports of the Tohoku Imperial University **21,** 256 (1932).
2. H. Kostron, Technisches Versuchsant Mitteilungen January, 17 (1932).
3. H. Kostron, Metallwirtschaft **12,** 473 (1933).
4. G. Sines and R. Carlson, ASTM Bulletin **180,** 35 (1952).
5. P.A. Blain, Sheet Metal Ind. **26,** 135 (1949).
6. P.A. Blain, Metal. Progress, 99 (1957).
7. J.O. Alamen, Prod. Eng., 121 (1950).
8. G.U. Oppel, Exp. Mech. **21,** 135 (1964).
9. T.R. Simes, S.G. Mellor, and D.A. Hills, J. Strain Anal. **19,** 135 (1984).
10. F.H. Vitovec, in *Microindentation Techniques in Materials Science and Engineering*, edited by P.J. Blau and B.R. Lawn (ASTM **889,** Philadelphia, PA, 1986), p. 175.
11. W.R. LaFontain, B. Yost, and C-Y. Li, J. Mater. Res. **5,** 776 (1990).
12. M.F. Doerner, D.S. Gardner, and W.D. Nix, J. Mater. Res. **1,** 845 (1986).
13. T.Y. Tsui, W.C. Oliver, and G.M. Pharr, J. Mater. Res. **11,** 752 (1996).
14. A. Bolshakov, W.C. Oliver, and G.M. Pharr, J. Mater. Res. **11,** 760 (1996).
15. A. Bolshakov and G.M. Pharr, J. Mater. Res. **13,** 1049 (1998).
16. S. Suresh and A.E. Giannakopoulos, Acta Mater. **46,** 5755 (1998).
17. B. Taljat and G.M. Pharr, in *Thin Films: Stresses and Mechanical Properties VIII*, edited by R. Vinci, O. Kraft, N. Moody, and E. Shaffer II (Mater. Res. Soc. Symp. Proc. **594,** Warrendale, PA, 2000), p. 519.
18. K.L. Johnson, J. Mech. Phys. Solids **18,** 115 (1970).
19. K.L. Johnson, *Contact Mechanics* (Cambridge University Press, Cambridge, United Kingdom, 1985).
20. H. Hertz, *Miscellaneous Papers*, edited by D.E. Jones and G.H. Schott (Macmillan, London, 1896), p. 163.
21. D. Tabor, *The Hardness of Metals* (Clarendon Press, Oxford, United Kingdom, 1951).
22. H.A. Francis, J. Eng. Mater. Technol. **98,** 272 (1976).
23. Y. Tirupataiah and G. Sundararajan, Metall. Trans. A **22A,** 2375 (1991).
24. The Aluminum Association, *Aluminum Standards and Data* (The Aluminum Association, New York, 1968), p. 28.
25. J.G. Swadener and G.M. Pharr, in *Thin Films: Stresses and Mechanical Properties VII*, edited by R. Vinci, O. Kraft, N. Moody, and E. Shaffer VIII (Mater. Res. Soc. Symp. Proc. **594,** Warrendale, PA, 2000), p. 525.
26. J.G. Swadener and G.M. Pharr, Philos. Mag. A **81,** 447 (2001).
27. J.S. Field and M.V. Swain, J. Mater. Res. **8,** 297 (1993).
28. W.C. Oliver and G.M. Pharr, J. Mater. Res. **7,** 1564 (1992).
29. Z. Mroz (private communication, Chicago, IL, August 31, 2000).
30. A.L. Norbury and T. Samuel, J. Iron Steel Inst. **117,** 673 (1928).
31. B. Taljat, T. Zacharia, and G.M. Pharr in *Fundamentals of Nanoindentation and Nanotribology*, edited by N.R. Moody, W.W. Gerberich, N. Burnham, and S.P. Baker (Mater. Res. Soc. Symp. Proc. **522,** Warrendale, PA, 1998), p. 33.

APPENDIX

Shift in location of initial yielding caused by large compressive biaxial stresses

Insight into the circumstances that cause the location of first yielding to switch from beneath the surface on the axis of symmetry to the contact periphery at the surface when large compressive biaxial stresses are applied can be obtained by examining the stress distribution for Hertzian contact. Using the Tresca yield criterion, Johnson showed that for $\nu_s = 0.3$, the maximum shear stress in the Hertzian contact problem is $|\sigma_r - \sigma_z|/2 = 0.465\,p_m$ at $z = 0.48\,a$.[18] The Hertzian solution for the stresses at the edge of contact gives $\sigma_\theta = -p_m(1 - 2\,\nu_s)/2$ and $\sigma_z = 0$ at $r = a$, $z = 0$ (see Ref. 19). Thus, when a compressive biaxial stress is superposed for the case of $\nu_s = 0.3$, the condition for yielding becomes $0.93\,p_m + \sigma^R \geqslant \sigma_y$ at $r = 0$, $z = 0.48\,a$, or $0.2\,p_m - \sigma^R \geqslant \sigma_y$ at $r = a$, $z = 0$. Initial yielding will then occur preferentially at the contact periphery rather than beneath the surface when $\sigma^R < -0.65\,\sigma_y$. The stress at the transition $\sigma^R =$

TABLE AI. Maximum biaxial stress (σ^R) for which yielding initiates at the edge of contact.

ν_s	0	0.1	0.2	0.3	0.4	0.5
σ^R/σ_y	−0.40	−0.46	−0.54	−0.65	−0.84	−1.0

$-0.65\,\sigma_y$ is within the range where the transition was observed in the finite element analysis, $-0.50\,\sigma_y > \sigma^R > -0.75\,\sigma_y$.[17]

For other values of ν_s, some differences can be expected. For a range of Poisson's ratio, the compressive biaxial stress for which the onset of yielding occurs at the edge of contact can be calculated by the same method. Results are listed in Table AI. Frictional effects would be expected to increase the magnitudes of these values. Therefore, the values in Table AI are probably conservative estimates of the range in which Eq. (7) is valid.